ADVANCED FUNCTIONAL MATERIALS

Supporting Information

for *Adv. Funct. Mater.*, DOI: 10.1002/adfm.201910491

Metals by Micro-Scale Additive Manufacturing: Comparison of Microstructure and Mechanical Properties

*Alain Reiser, Lukas Koch, Kathleen A. Dunn, Toshiki Matsuura, Futoshi Iwata, Ofer Fogel, Zvi Kotler, Nanjia Zhou, Kristin Charipar, Alberto Piqué, Patrik Rohner, Dimos Poulikakos, Sanghyeon Lee, Seung Kwon Seol, Ivo Utke, Cathelijn van Nisselroy, Tomaso Zambelli, Jeffrey M. Wheeler, and Ralph Spolenak**

Supporting Information

Metals by micro-scale additive manufacturing: comparison of microstructure and mechanical properties

Alain Reiser, Lukas Koch, Kathleen A. Dunn, Toshiki Matsuura, Futoshi Iwata, Ofer Fogel, Zvi Kotler, Nanjia Zhou, Kristin Charipar, Alberto Piqué, Patrik Rohner, Dimos Poulikakos, Sanghyeon Lee, Seung K. Seol, Ivo Utke, Cathelijn van Nisselroy, Tomaso Zambelli, Jeffrey M. Wheeler, Ralph Spolenak*

*To whom correspondence should be addressed; E-mail: ralph.spolenak@mat.ethz.ch

S1 Morphology

S1.1 LIFT (melt)

Figure S1 shows LIFT structures printed from a Cu as well as a Au donor film.

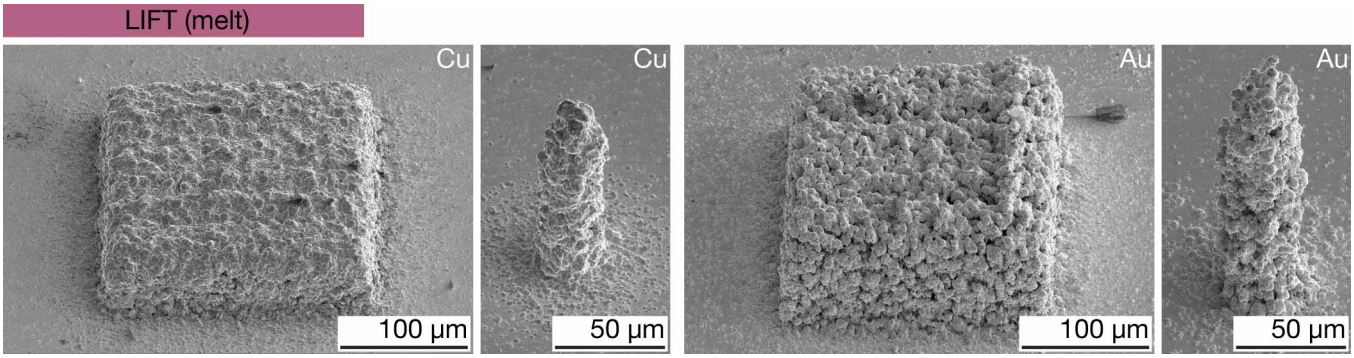

Figure S1: **Morphology of LIFT-printed Cu and Au.** SE micrographs of representative pads and pillars printed from either a Cu (left) or a Au (right) donor thin film. Image tilts: 45° for pads and 55° for pillars.

S1.2 Distortion upon annealing

Au pillars and pads printed by EHDP and LAEPD both underwent pronounced inhomogeneous shrinkage that resulted in wrinkled pillars and often poor adhesion of the annealed pads. In contrast, DIW and LIFT (ink) deposited Ag structures, especially pillars, showed a more isotropic volume loss (although cracking is evident in annealed DIW (N.) pads). The precise reason for the observed difference is unknown. The most obvious distinctions between inhomogeneously and homogeneously shrunken pillars are their size ($\approx$2 µm dia. for the inhomogeneous pillars versus $\approx$10 – 40 µm for the homogeneous pillars) and their material (Au and Ag, respectively). While the metal itself is probably secondary, the size might have a very simple effect: in small structures, small-scale inhomogeneities upon densification are proportionally larger compared to the size of the whole structure, and have thus a more profound effect on the resulting overall geometry. In larger structures, the same inhomogeneities are probably averaged or simply less obvious. However, as structures were printed by different methods and the as-deposited densities probably differ as well, no general conclusion should be drawn from this observation. In any case, the management of shrinkage and accompanied distortions will likely be a challenge for all ink-based methods in more complex geometries than those shown in this study.

S1.3 Effect of different printing strategies

Printing strategies differ between the individual techniques. For example, pillars printed by DIW, LAEPD, MCED and the FluidFM were deposited with a width of a single voxel, i.e. without in-plane hatching but simple out-of-plane growth. In contrast, pillars printed by EHDP, LIFT (melt), EHD-RP, FIBID, FEBID and cryo-FEBID are built from hatched layers. With a resolution $\ll$1 µm this strategy enables control of the micropillar's cross-section (Figure S2).

Most pads were printed with multiple hatched layers, but pads by LIFT (ink) and MCED are single entities (LIFT (ink): a single sheet of ink, MCED: a deposit grown with a large capillary). The advantage of adapting to various shapes without the need for hatching within single layers is interesting: tuning the shape and size of single voxels to accommodate certain geometries with as few voxels as possible is an advantage which simplifies and accelerates the printing of the here demanded geometries and typically decreases the surface roughness (see pads by LIFT (ink) or MCED). Nevertheless, the surface finish and overall fidelity of real-life structures built from many voxels cannot be interpolated from these results. Especially in case of MCED, this approach is clearly limited to geometries as simple as the ones presented here. In contrast, LIFT (ink) has demonstrated the transfer of complexly shaped, large sheets that enable smooth layers also for intricate layer designs[1]. Furthermore, smooth joining of multiple voxels has been demonstrated[2].

S2 Microstructure and chemical composition

Figure S3 presents cross-sections of pads imaged at low magnification. Figure S4 compares the microstructures of annealed inks in different geometries. For each method, the shown pads and pillars were annealed with the same annealing procedures. While some microstructures compare well (DIW (N.), EHDP), others differ between pads and pillars, presumably due to differences

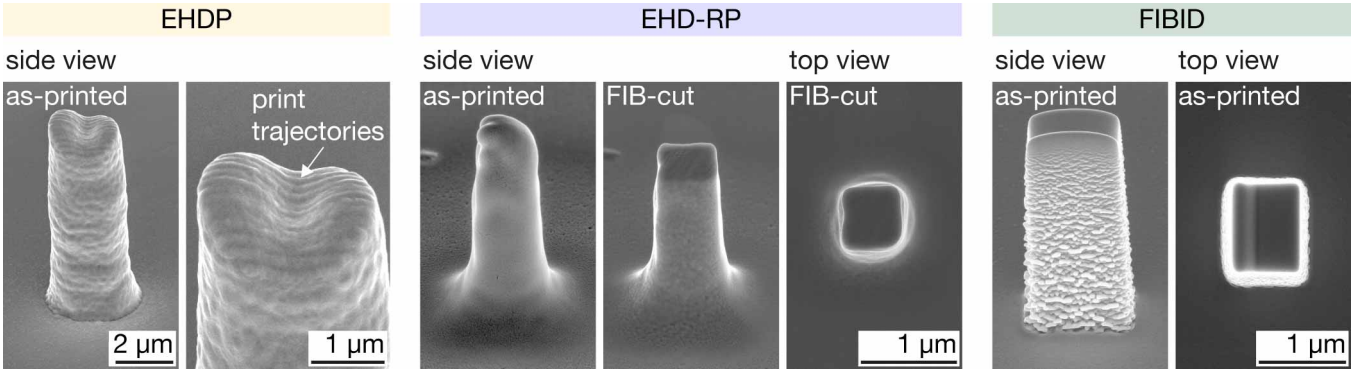

Figure S2: **High-resolution in-plane hatching.** The techniques with a resolution $\ll$1 µm enable shape control of printed pillars' cross-sections. In the case of EHDP, pillars are round, but the visible print trajectories indicate the in-plane hatching. Pillars by EDH-RP and FIBID (as well as FEBID, not shown) are square due to the quadratic hatch patterns used. A FIB-cut pillar is shown for EHD-RP to highlight the quadratic cross-section. Tilt of side-view images: 55°.

in local temperatures and local mechanical constraints. All shown pillars feature radial gradients in porosity, with some pillars even being hollow (EHDP, LIFT (ink)). In contrast, the microstructure of pads is typically more homogeneous (at least in the center of the pads, where the cross-sections were cut – we have not studied the edges of the large DIW and LIFT (ink) pads). As an exception, the center of the EHDP pads delaminated upon annealing.

Figure S5 summarizes the SEM EDX analysis performed on printed pads. EDX spectra were recorded with identical acquisition conditions from a printed pad (blue, same batch of samples presented in Figure S3) and the substrate (red). We refrain from a quantitative analysis of the presented data – especially of the carbon and oxygen content – for the following reasons: first, quantification of the light elements (C, N, O in our case) by EDX is unreliable. Second, C is always co-deposited by the electron beam during analysis. Third, the variation in geometry and density of the pads does not allow for a direct comparison between the techniques, and additionally, makes consistent decoupling signals from the printed geometries and the substrates impossible. Nevertheless, we cite some numbers in the following paragraphs – please note that these are at best approximate values and that the signals from the substrate were not subtracted for this analysis.

The following qualitative statements can be made: all as-deposited colloidal inks contain carbon. Upon annealing, this amount is often not significantly reduced (from ≈50 at.% to ≈40 at.% for both DIW inks annealed at 300 and 450 °C, respectively; from ≈70 at.% to ≈45 at.% for EHDP pads annealed at 400 °C in O_2 atmosphere; no reduction upon annealing for LAEPD pads (≈50 at.%)). Thus, post-print procedures that specifically target the removal of carbon should be studied if a pronounced reduction in carbon content is desired. Similarly, as-deposited FIBID and FEBID pads contain large amounts of carbon (≈55 – 65 at.%). Additionally, FIBID structures contain Ga (≈15 at.%), and FEBID pads contain oxygen (≈35 at.%). Routines for purification of FEBID and FIBID structures exist[3–7] and need to be applied with most precursor compounds if high metal content is required in the final deposits. In contrast, electrochemically grown pads are mostly pure Cu – a C-K peak is detected for pads printed by MCED, FluidFM and EHD-RP, but in all cases, the same peak is present in the spectra of the substrates, indicating a general C contamination of the samples rather than a specific contamination of the printed structures.

S2.1 Laser-induced fusing of Au particles in LAEPD

We hypothesize that electrophoretically printed Au nanoparticles are fused upon laser-assisted deposition, resulting in the high strength observed for as-deposited LAEPD samples. The hypothesis is supported by the previous demonstration of laser-induced sintering of Au particles of the same size in air at lower power densities than those used by LAEPD[8]. Yet, in LAEPD one should expect a mediation of the local temperature by the surrounding liquid which would forbid temperatures that surpass the boiling point of water (as boiling was not observed). Because such low temperatures would inhibit the fusion of particles despite the melting point depression in small Au particles[9], the details of the microstructure as well as the related deposition mechanism will need closer attention in future studies.

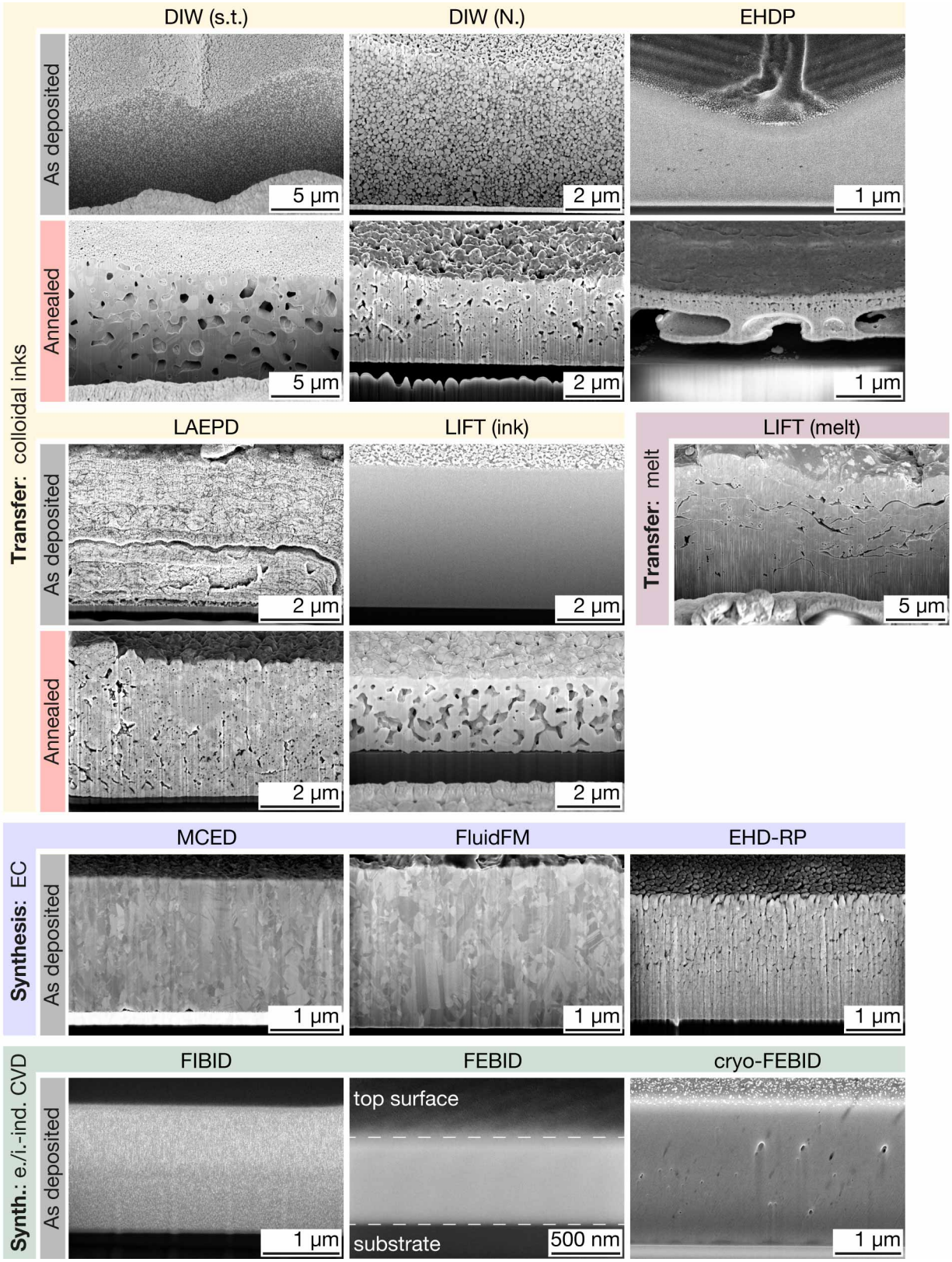

Figure S3: **Microstructure of printed pads.** Representative cross-section micrographs of printed pads at lower magnification. The as-printed and annealed pads of EHDP and LIFT (ink) had different as-deposited thicknesses (hence no shrinkage can be concluded from these images). The cross-section of the as-deposited EHDP pad was made after indentation (hence the triangular indent at its surface). All images are tilt-corrected.

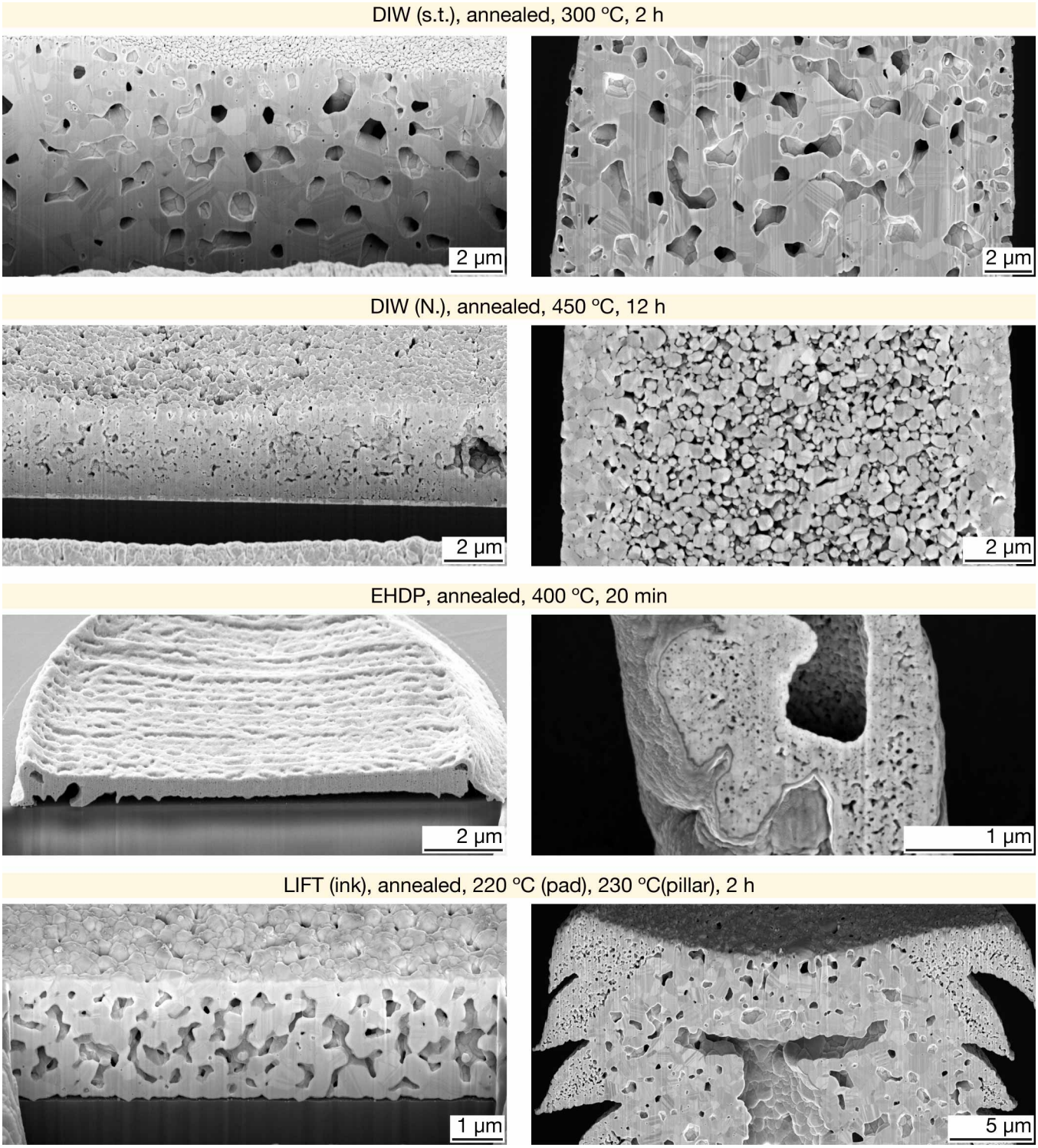

Figure S4: **Microstructure of annealed pads and pillars printed from colloidal inks / suspensions.** FIB-cut cross-sections of representative pads and pillars printed with various colloid transfer techniques. Pads and pillars from the same techniques were annealed with the same annealing procedure.

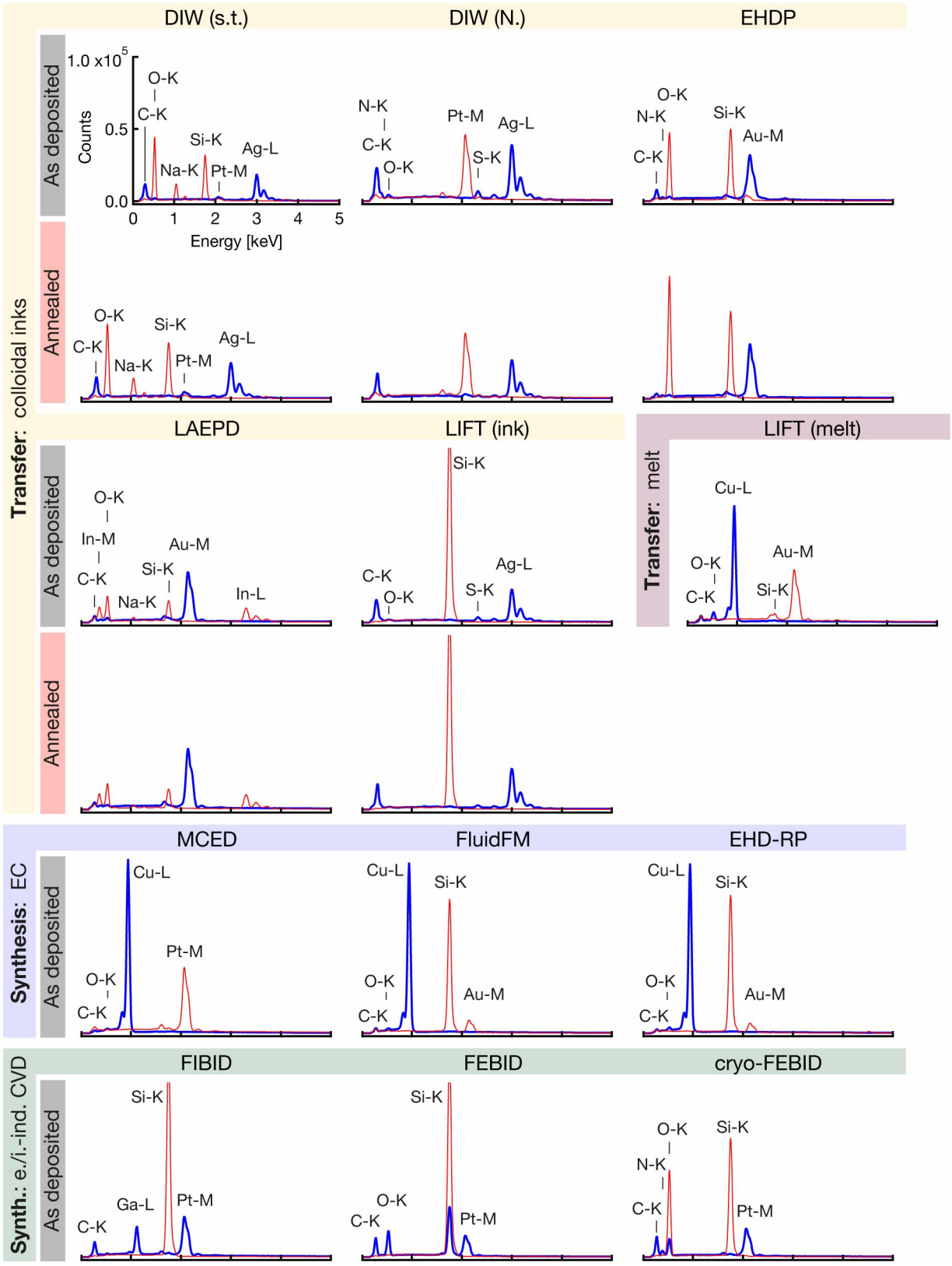

Figure S5: **EDX analysis of printed pads.** EDX spectra of printed pads (blue) and respective substrates (red) acquired with identical parameters. The scale of all graphs is identical to the axes in the DIW (s.t.) graph.

S3 Mechanical data for all tested samples of all techniques

Table S1 lists the averaged values of Young's modulus E, hardness H and yield stress $\sigma_{0.07}$ of the metals printed by all studied techniques. In addition, Figures S6 – S21 summarize the mechanical data collected for all tested AM methods presented in this manuscript. The data is organized as follows (Figure S6): one or two figures per method present all analyzed mechanical data and representative micrographs of the materials' microstructures. In each figure, the data is grouped by annealing state. The left column presents nanoindentation data collected from printed pads, the right column microcompression data from printed pillars. Each graph is accompanied by a representative cross-section micrograph from one of the pads and pillars from the respective batch of samples. The nanoindentation graph shows Young's modulus (red) and hardness (blue) measured as a function of depth. The graph plots an averaged curve (bold line, with the shaded area representing the standard deviation) of all recorded curves (dashed lines). E and H values reported in the manuscript were extracted from the depth range highlighted in the average curves. The microcompression graph displays all measured stress-strain curves (using the average diameter of the deformed portion of the pillars). One representative curve is highlighted for better visibility.

S3.1 Hardness versus strength of as-deposited DIW inks

As a deviation from the expected relation of hardness to strength in solids, we measure a pronouncedly higher strength of DIW inks upon microcompression compared to the hardness derived from nanoindentation of the same materials ($\sigma_{0.07}$: 0.256 – 0.315 GPa and H: 0.062 – 0.141 GPa, Figures S6 and S8). For dense solids, indentation hardness H is $\approx$3 times the yield strength σ [10]. For porous solids, the constraint factor can reduce to unity, i.e. $H = \sigma$, but H never becomes smaller than σ. However, as-printed inks are clearly not solids, but rather granular media, as they are composed of discrete, noncohesive particles. Thus, strength is not necessarily related to plastic deformation of a solid, but rather the flow of individual particles under shear loading. While an analysis of the mechanics of these materials is outside the scope of this paper, we can speculate about the origins of the observed difference. Due to the interlocking of colloids, the necessary yield stresses for deformation is a function of the applied normal stresses [11]. As the stress fields below a flat punch (microcompression) and a sharp pyramid (indentation) are very different, the resulting contact pressures detected with the two methods might differ. Additionally, the probe size in nanoindentation is comparable to the particle size and inter-particle spacing of the probed medium (indenter radius $\approx$50 nm, large particles $\approx$250 nm), whereas it is larger in microcompression (punch diameter $>$ pillar diameter, i.e. $>$10 µm). Thus, the two methods may potentially probe different deformation mechanisms. Interestingly, this difference is only observed for DIW inks, hinting towards an influence of the particle shape, the respective binder phase, or the particle size distribution.

S3.2 Nanoindentation: thickness and roughness of pads

Table S2 lists the minimal thickness and the maximal roughness of the tested pads. The thickness of all tested pads was assessed by confocal optical profilometry. Note that for most techniques, pads may vary in thickness by several tens of percent. Pads of different thickness were either motivated by minimization of printing time (printing only a few thick pads for verification of results obtained from thinner pads), were caused by different annealing protocols between different samples of a technique, or were simply the result of a variation of deposition parameters during a deposition session. As only low thicknesses are potentially problematic for nanoindentation, only the lowest thickness of all pads deposited by each technique is reported. Roughness was measured from AFM scans of the roughest of all tested samples of a given technique, as judged from SEM images. In LAEPD, the depth range for analysis was limited by a finite pad size.

Table S1: E, H **and** $\sigma_{0.07}$ **data.** Averaged values for Young's modulus E, hardness H and yield stress $\sigma_{0.07}$ for as-deposited (ad.) and annealed samples.

Technique	Nanoindentation		Microcompression	
	E [GPa]	H [GPa]	E [GPa]	$\sigma_{0.07}$ [GPa]
DIW (s.t.)				
ad. (100 °C, 0.5 h)	12.6 ± 3.2	0.141 ± 0.051	33.3 ± 4.1	0.265 ± 0.039
300 °C, 0.5 h	41.1 ± 9.5	0.461 ± 0.181	35.7 ± 0.7	0.289 ± 0.027
300 °C, 2 h	31.1 ± 10.0	0.435 ± 0.123	42.1 ± 3.8	0.168 ± 0.008
DIW (N.)				
ad.	4.56 ± 1.00	0.0665 ± 0.0135	35.7 ± 2.7	0.315 ± 0.015
450 °C, 12 h	49.2 ± 12.9	0.855 ± 0.211	65.7 ± 2.7	0.422 ± 0.028
EHDP				
ad.	0.521 ± 0.160	0.0480 ± 0.0154	1.09 ± 0.14	0.0168 ± 0.0017
400 °C, 20 min	not analyzed	not analyzed	31.3 ± 0.4	0.246 ± 0.058
400 °C, 20 min, pillars ⌀≈350 nm	N/A	N/A	39.8 ± 8.8	0.411 ± 0.057
LAEPD				
ad.	9.09 ± 5.95	0.369 ± 0.321	7.29 ± 4.06	0.146 ± 0.104
300 °C, 1 h	54.2 ± 12.5	1.42 ± 0.41	47.1 ± 8.5	0.366 ± 0.056
LIFT (ink)				
ad.	1.94 ± 0.07	0.108 ± 0.004	1.16 ± 0.01	0.0125 ± 0.0014
200 °C, 1 h	36.4 ± 2.5	0.661 ± 0.074	12.8 ± 0.9	0.0880 ± 0.0008
220 (pads) / 230 °C (pillars), 2 h	31.0 ± 3.5	0.400 ± 0.072	26.9 ± 0.4	0.118 ± 0.004
LIFT (melt)				
Cu	73.2 ± 10.4	1.66 ± 0.37	49.8 ± 7.4	0.415 ± 0.028
Au	24.3 ± 10.1	0.293 ± 0.235	28.3 ± 3.5	0.186 ± 0.020
MCED				
ad.	121.8 ± 7.4	2.71 ± 0.36	114.2 ± 3.6	0.774 ± 0.104
FluidFM				
ad.	138.4 ± 18.7	2.28 ± 0.45	134 ± 11	0.962 ± 0.026
EHD-RP				
ad.	80.4 ± 17.9	2.22 ± 0.82	81.7 ± 8.4	1.10 ± 0.12
ad., pillars ⌀≈170 nm	N/A	N/A	88.4	1.38 ± 0.06
FIBID				
ad.	140.0 ± 7.9	9.42 ± 0.11	95.3 ± 9.5	2.64 ± 0.25
FEBID				
ad.	75.5 ± 1.6	6.01 ± 0.32	59.3 ± 3.9	2.65 ± 0.04
cryo-FEBID				
ad.	13.8 ± 1.0	0.843 ± 0.074	3.85 ± 0.93	0.100 ± 0.059

Table S2: **Thickness and roughness of pads,** as well as depth range used for nanoindentation analysis. Values of min. thickness and RMS roughness are rounded. An X in *Thickness variation* indicates pads of thicknesses that differ by more than 20% between pads or within single pads.

Technique	Min. thickness [nm]	RMS roughness [nm]	Analysis depth range [nm]
DIW (s.t.)	6000	340	1000 – 1700
DIW (N.)	1300	150	400 – 600
EHDP, ad.	1200	100	150 – 300
LAEDP	2500	110	100 – 200
LIFT (ink)	2200	70	200 – 350
LIFT (melt), Cu	40000	1590	2500 – 5400
LIFT (melt), Au	57000	4330	6100 – 14800
MCED	1400	13	100 – 215
FluidFM	1500	120	260 – 400
EHD-RP	1400	50	240 – 500
FIBID	400	1	75 – 115
FEBID	550	4	60 – 80
cryo-FEBID	2900	20	100 – 300

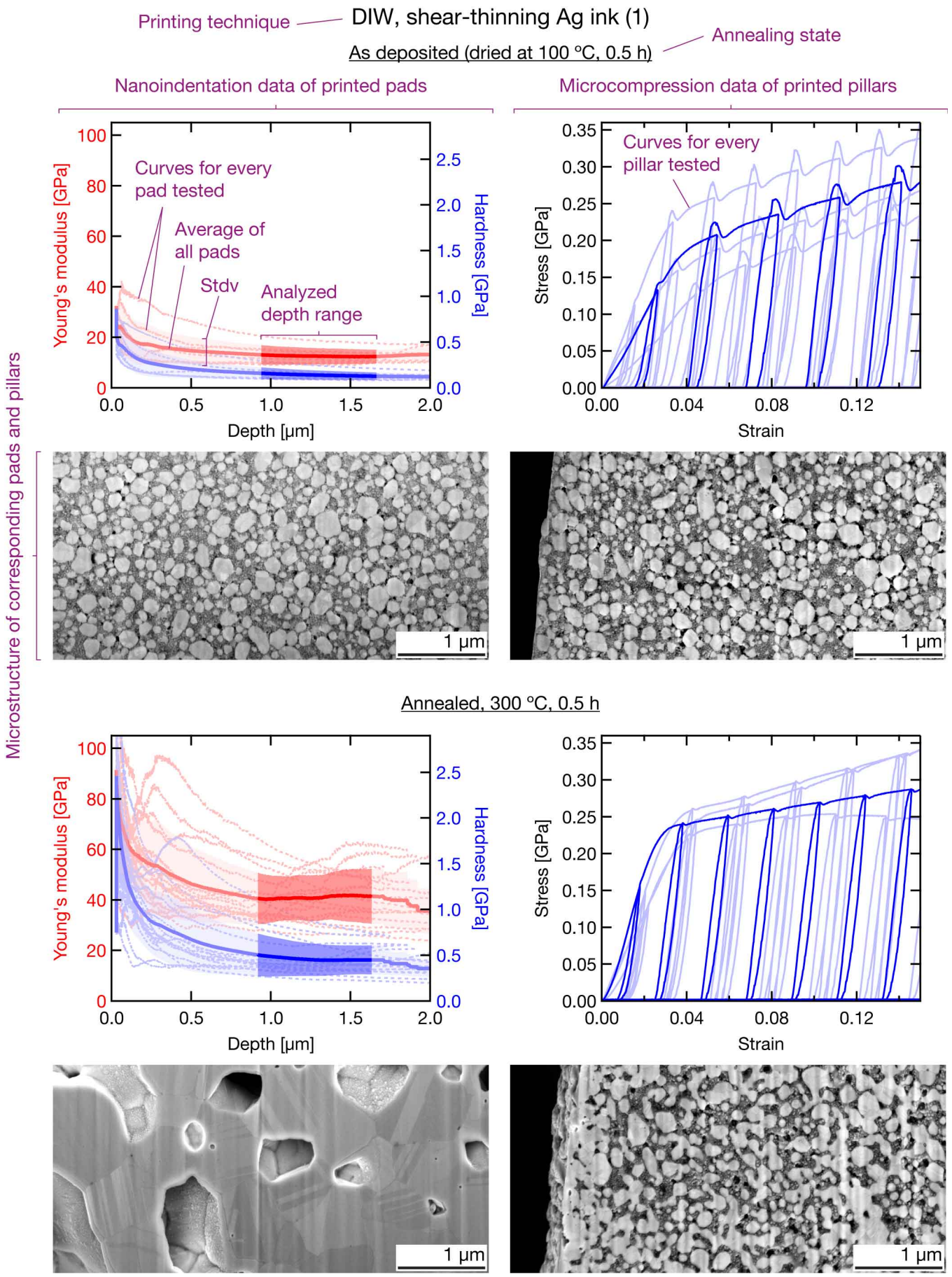

Figure S6: Direct ink writing, shear-thinning Ag ink (DIW (s.t.)).

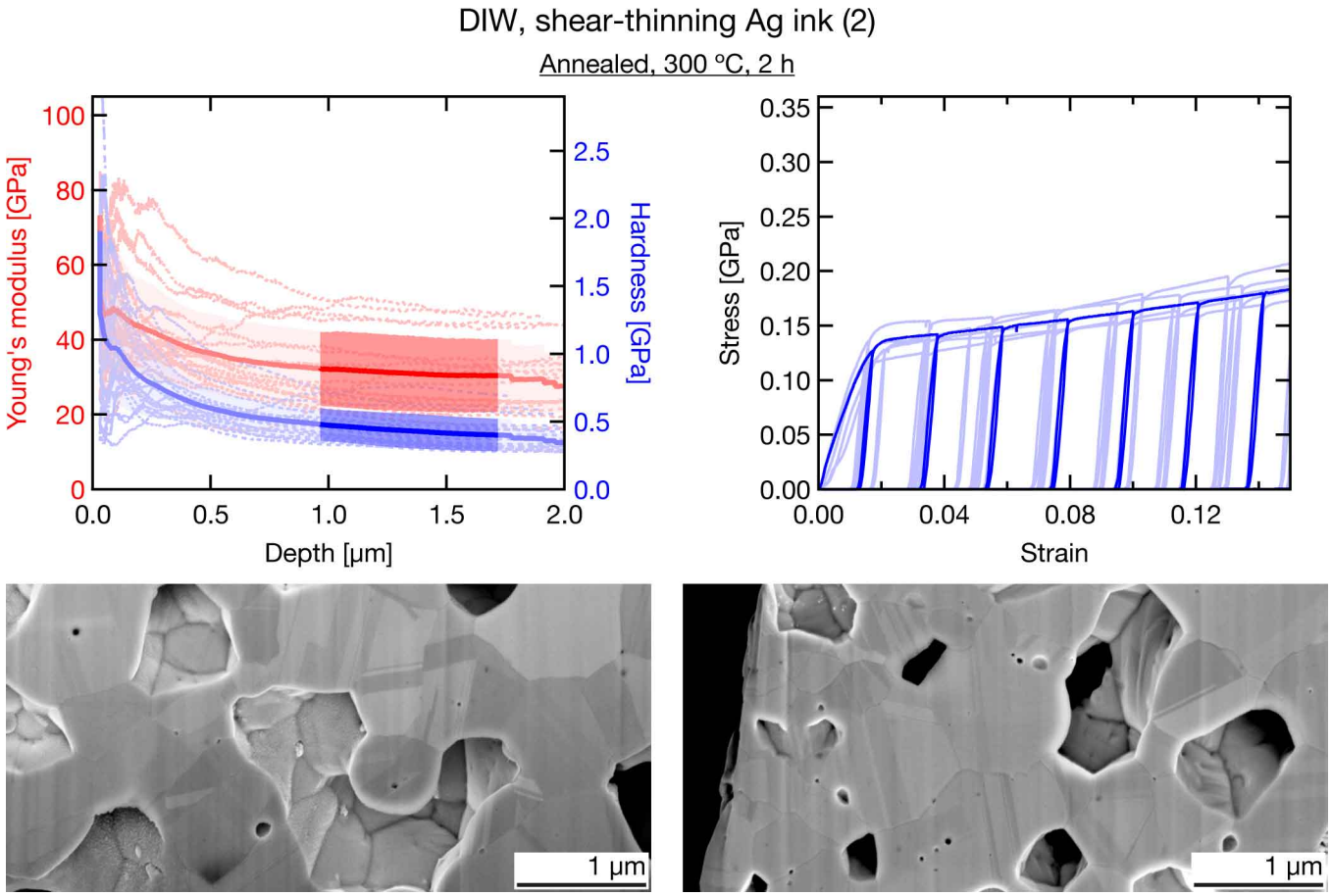

Figure S7: Direct ink writing, shear-thinning Ag ink (DIW (s.t.)).

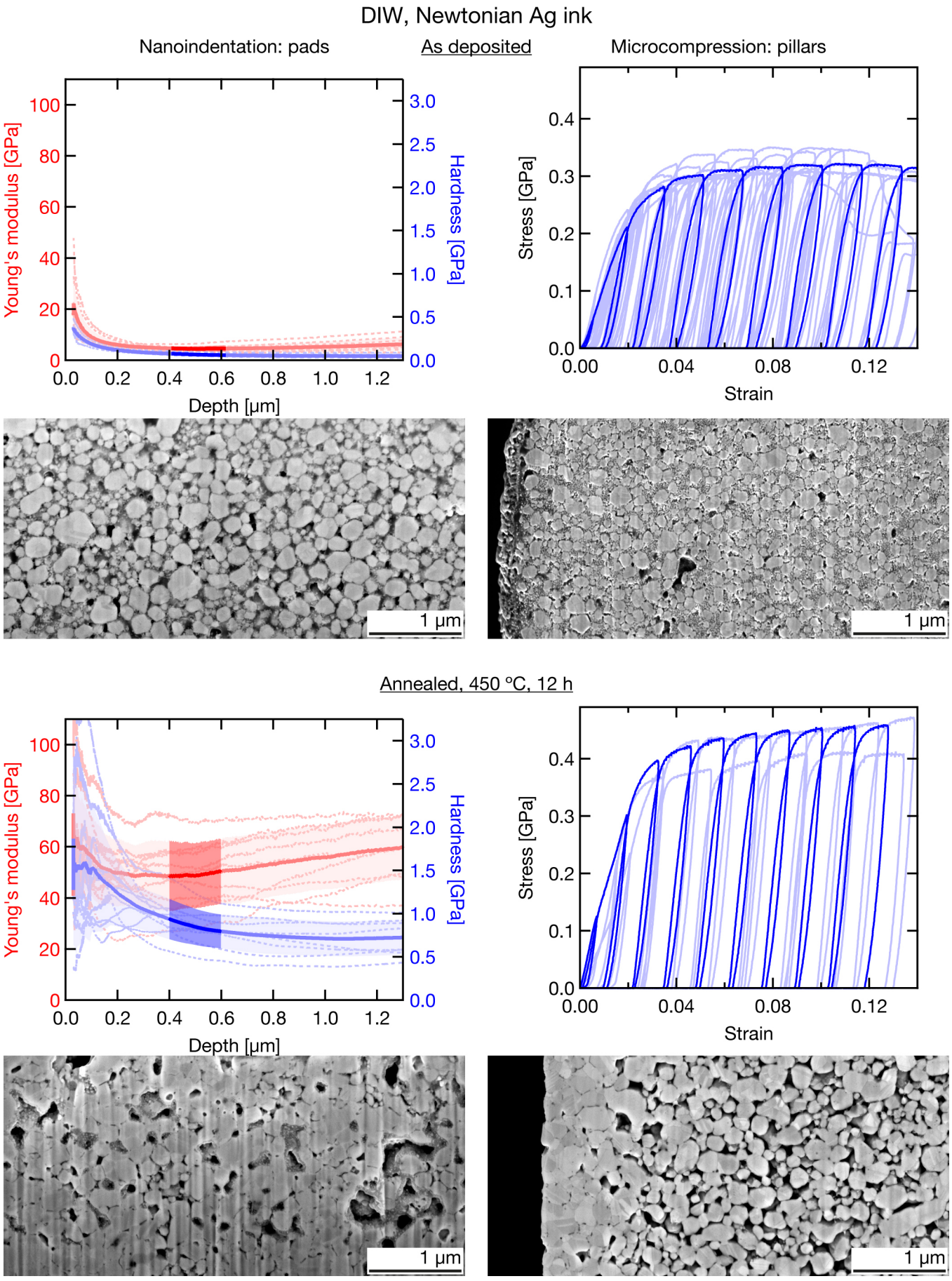

Figure S8: Direct ink writing, Newtonian Ag ink (DIW (N.)).

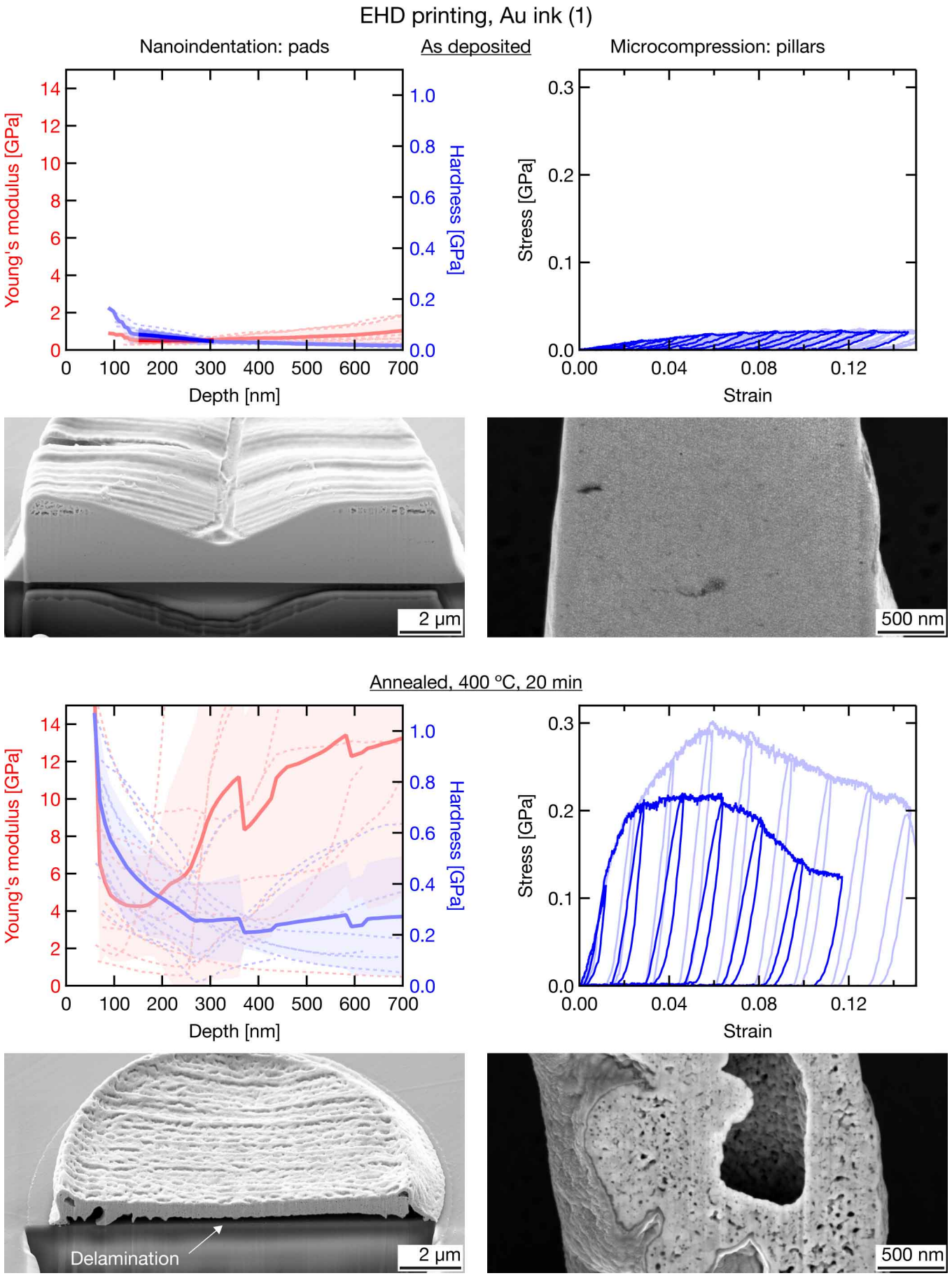

Figure S9: Electrohydrodynamic printing, Au ink (EHDP). The as-deposited pad was indented before taking the image, hence the pyramidal indent. Nanoindentation data of annealed pads was not analyzed, as the large-scale delamination of the pads upon annealing prevented the collection of representative data.

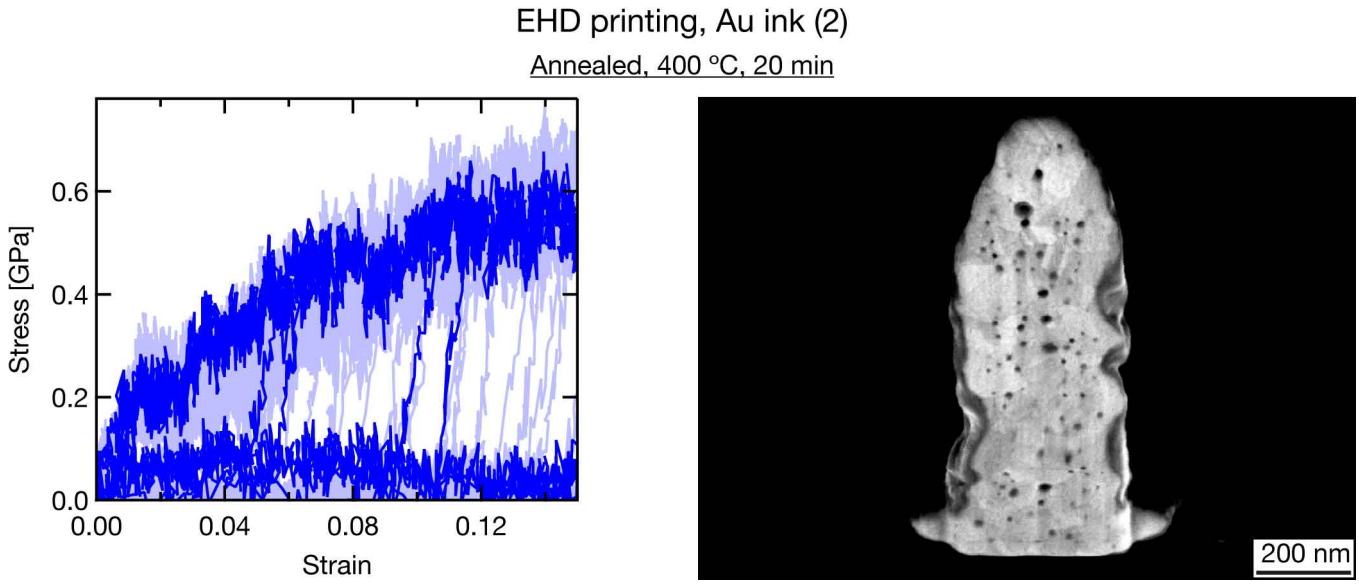

Figure S10: Electrohydrodynamic printing, Au ink (EHDP). Microcompression data and representative cross-section of annealed pillars 300 – 350 nm in diameter.

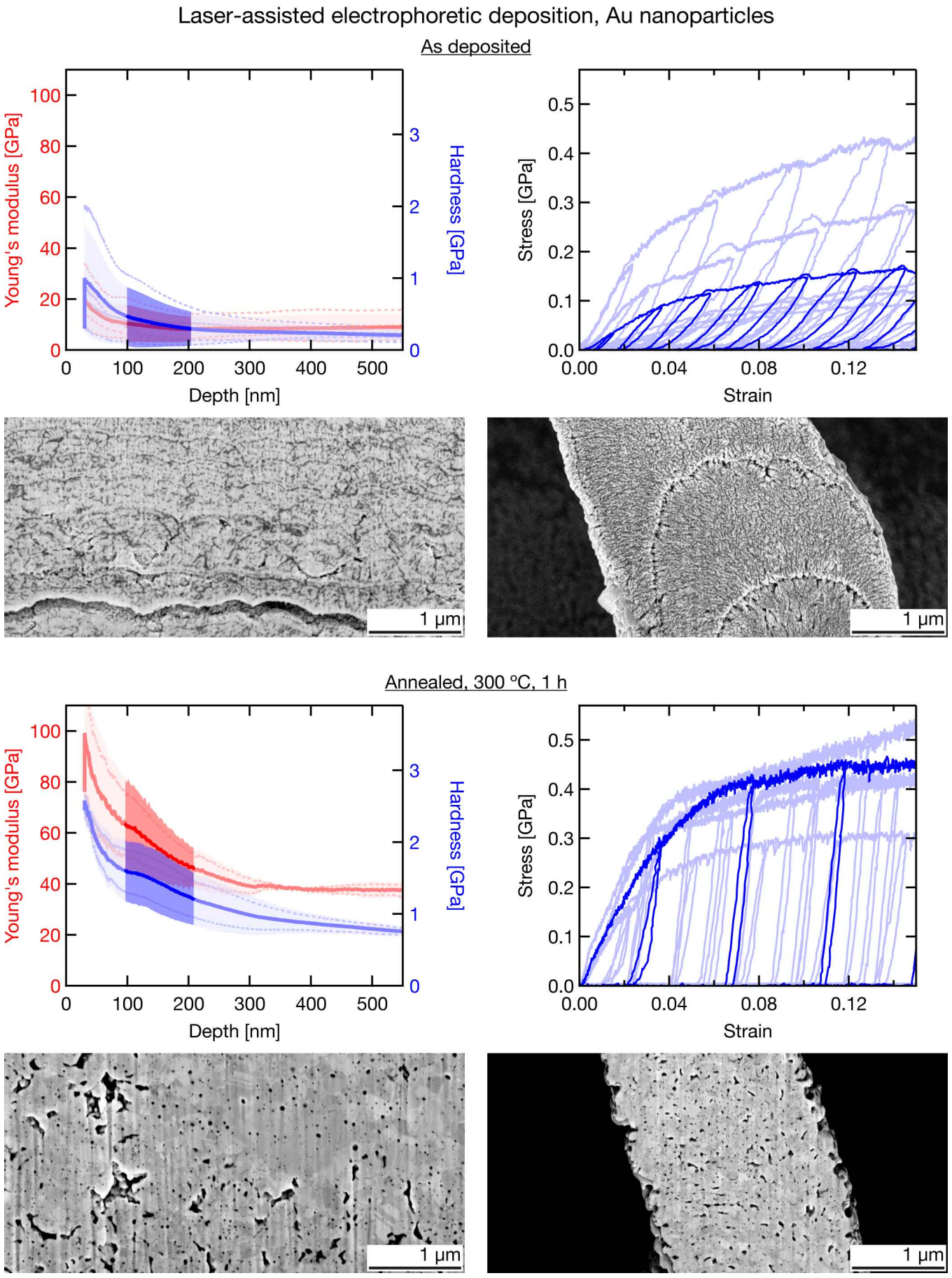

Figure S11: Laser-assisted electrophoretic deposition (LAEPD), Au nanoparticles.

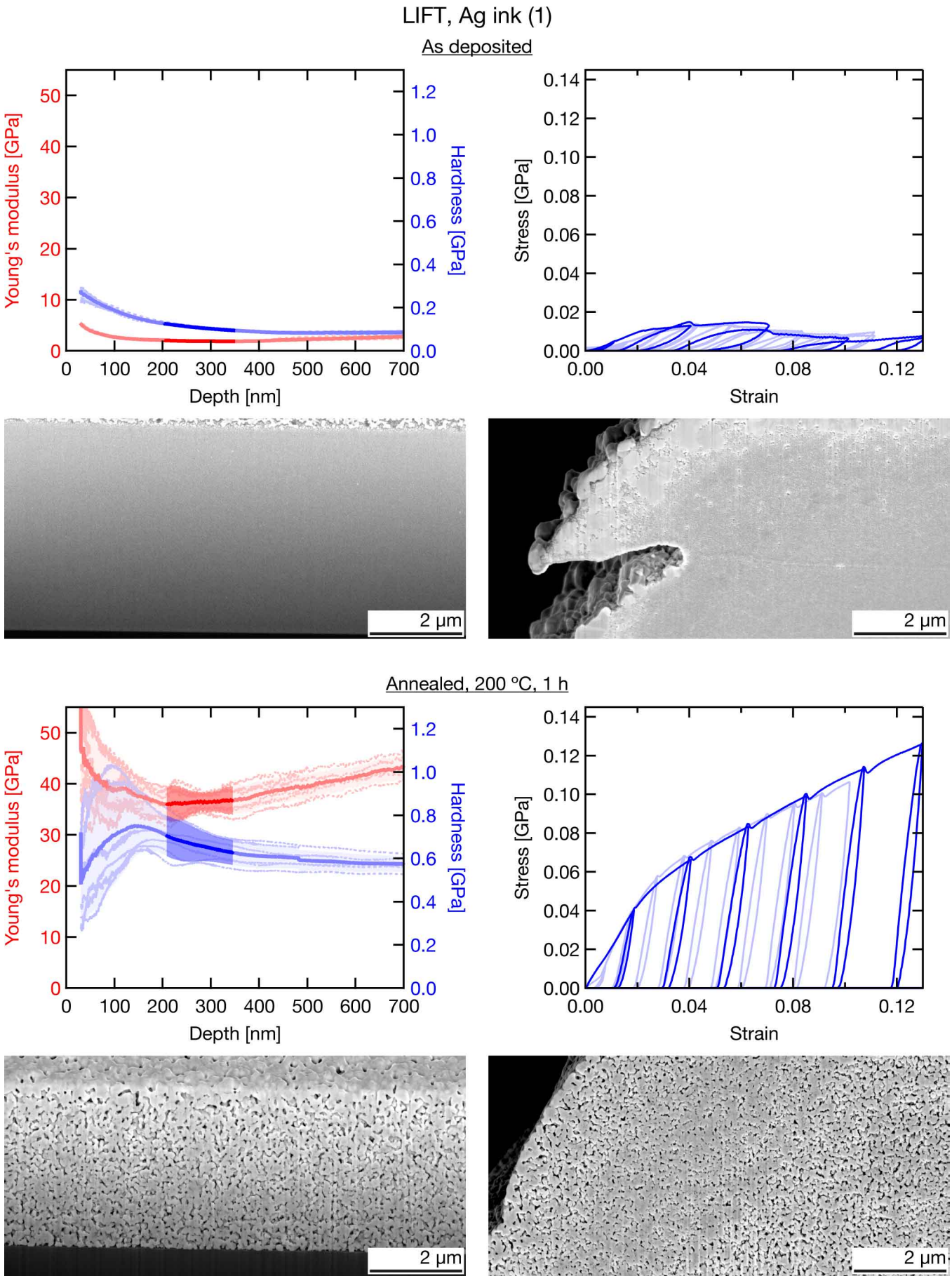

Figure S12: Laser-induced forward transfer of Ag ink (LIFT (ink)).

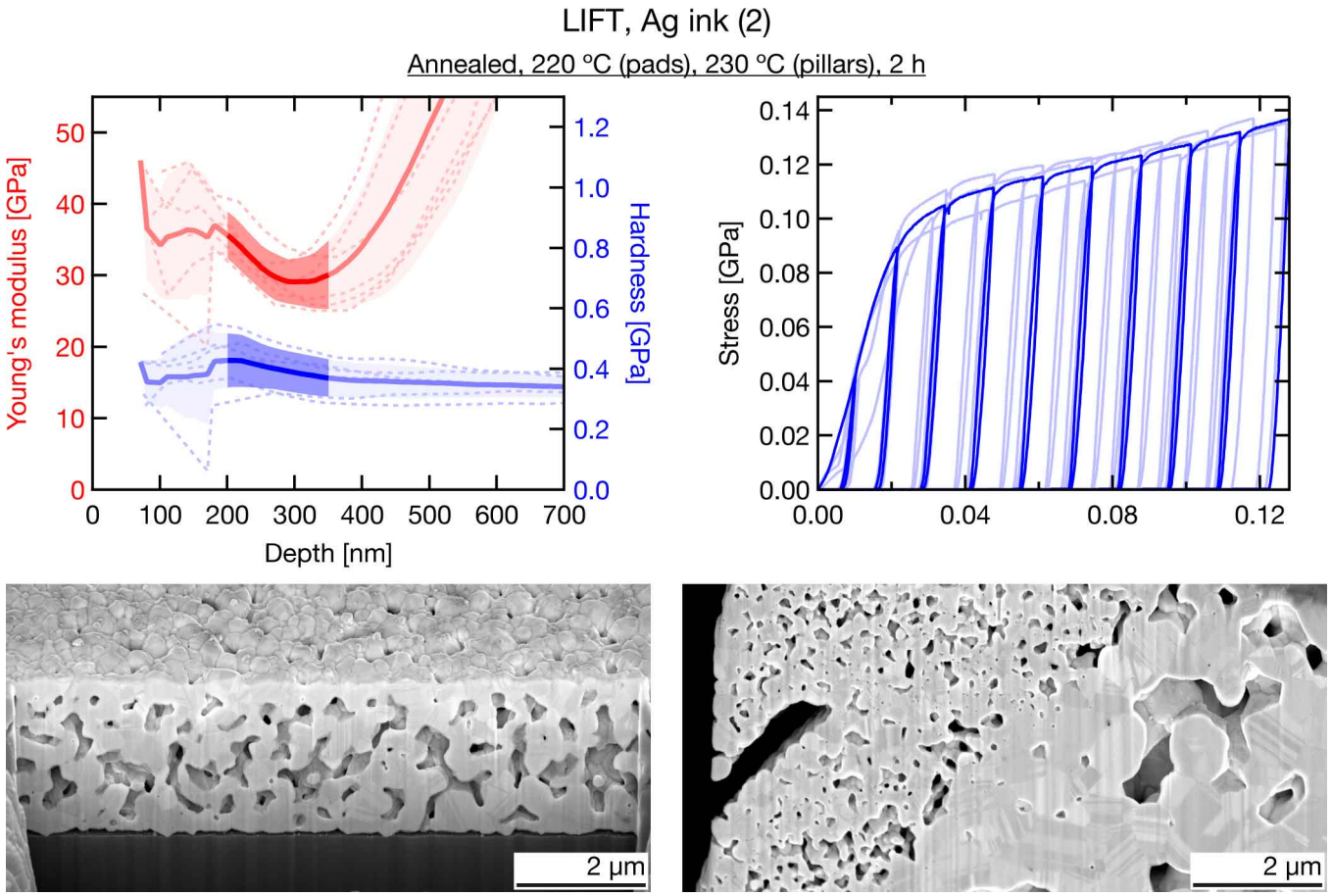

Figure S13: Laser-induced forward transfer of Ag ink (LIFT (ink)).

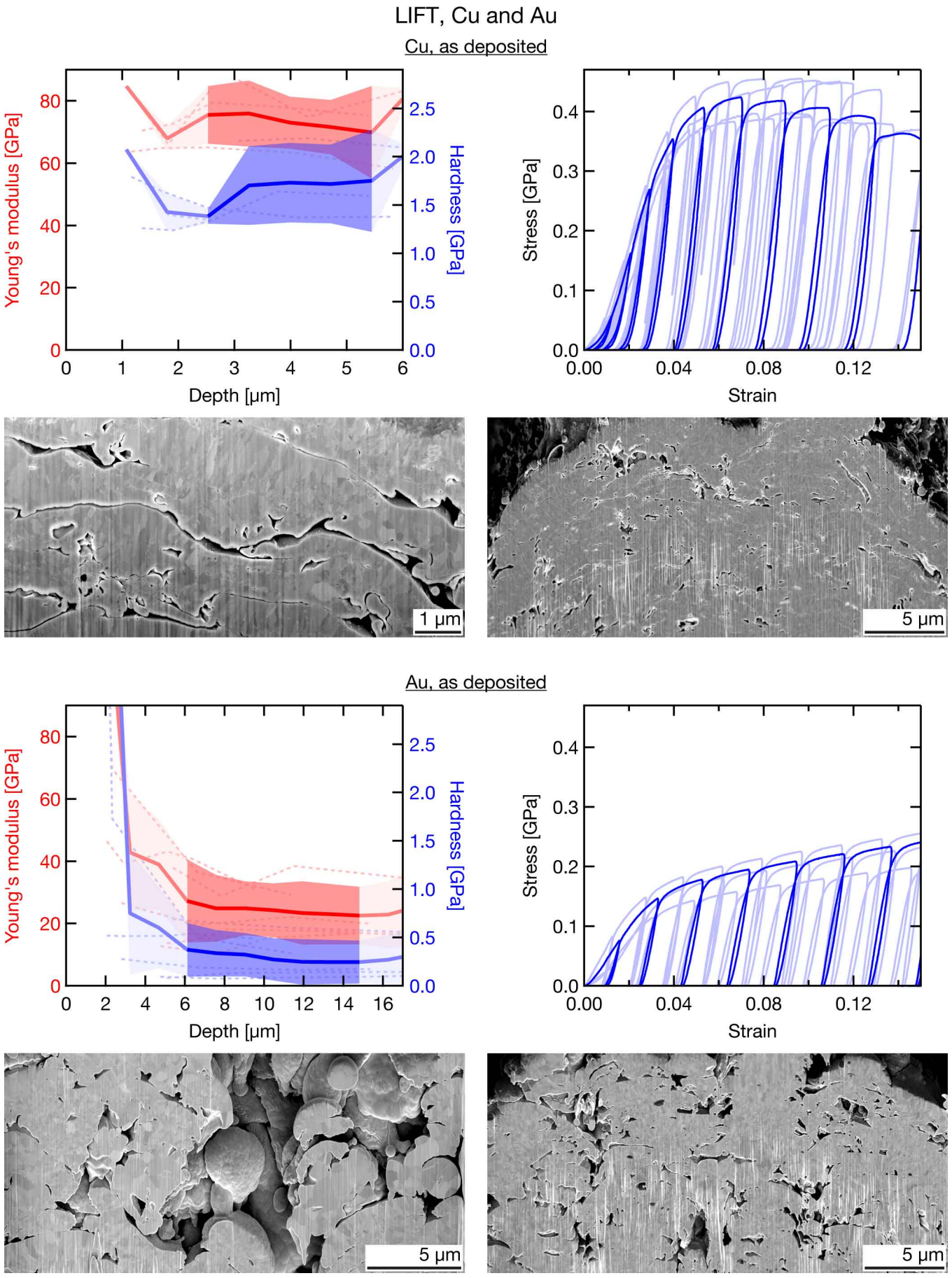

Figure S14: Laser-induced forward transfer of Cu and Au (LIFT).

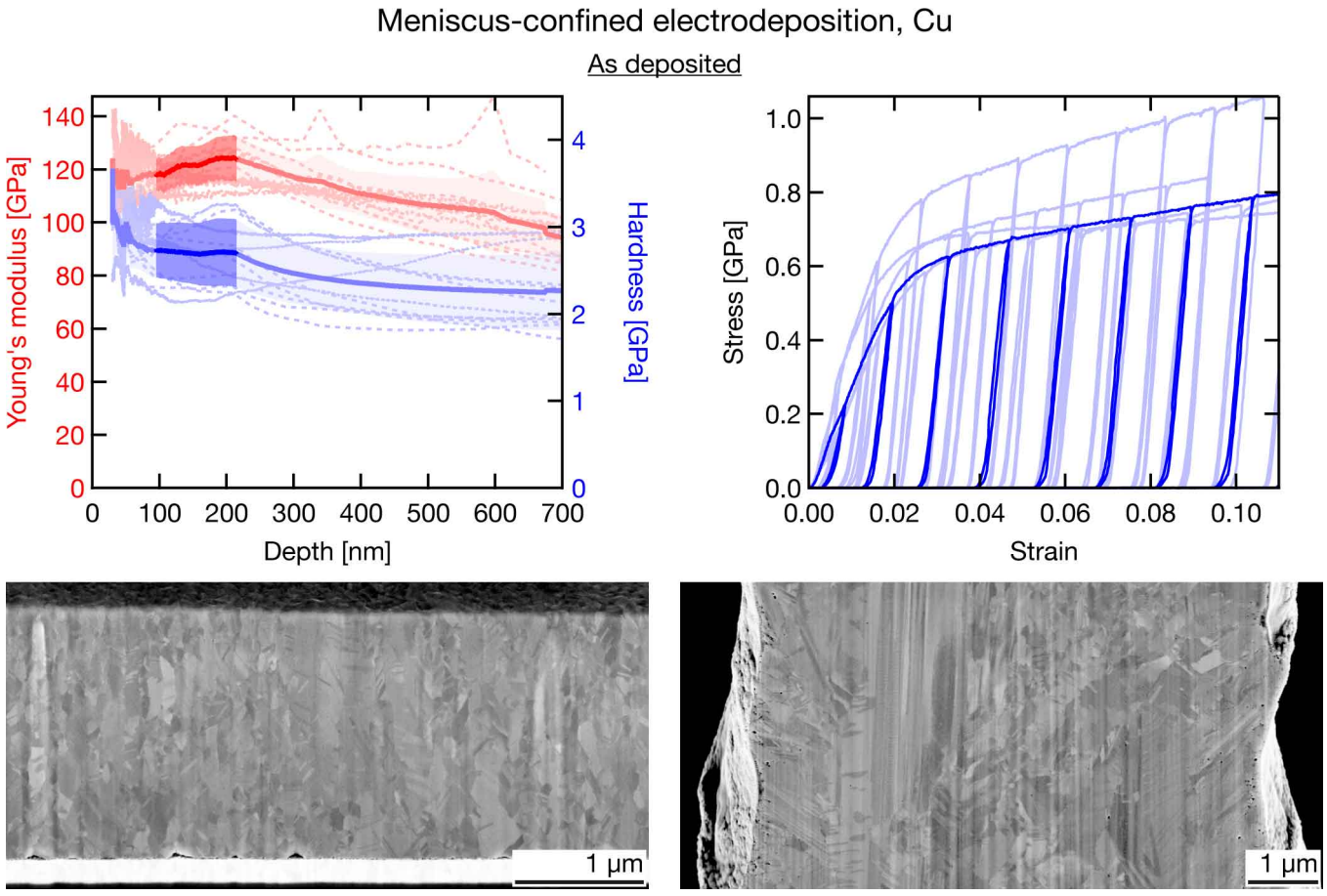

Figure S15: Meniscus-confined electrodeposition (MCED) of Cu.

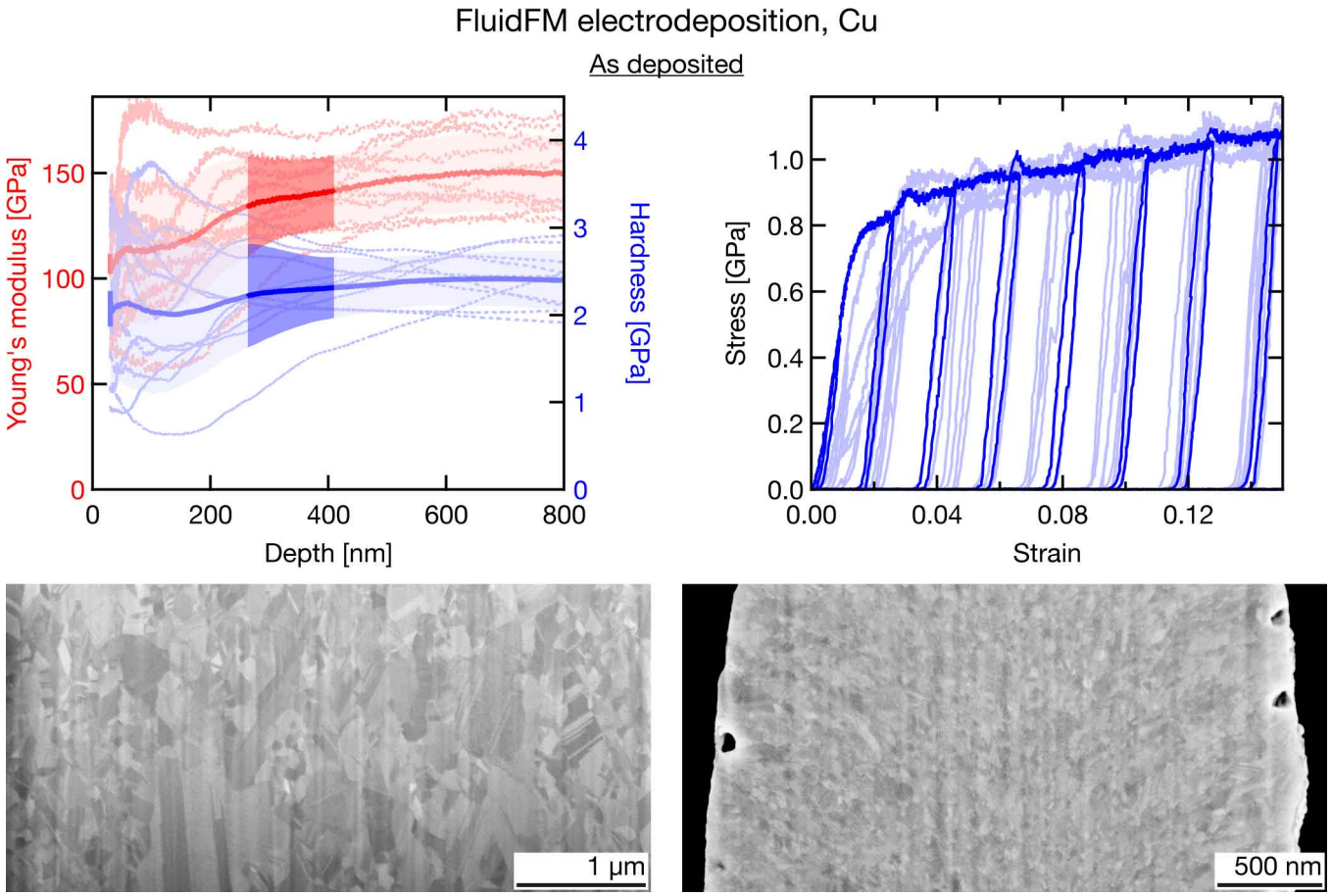

Figure S16: FluidFM electrodeposition of Cu.

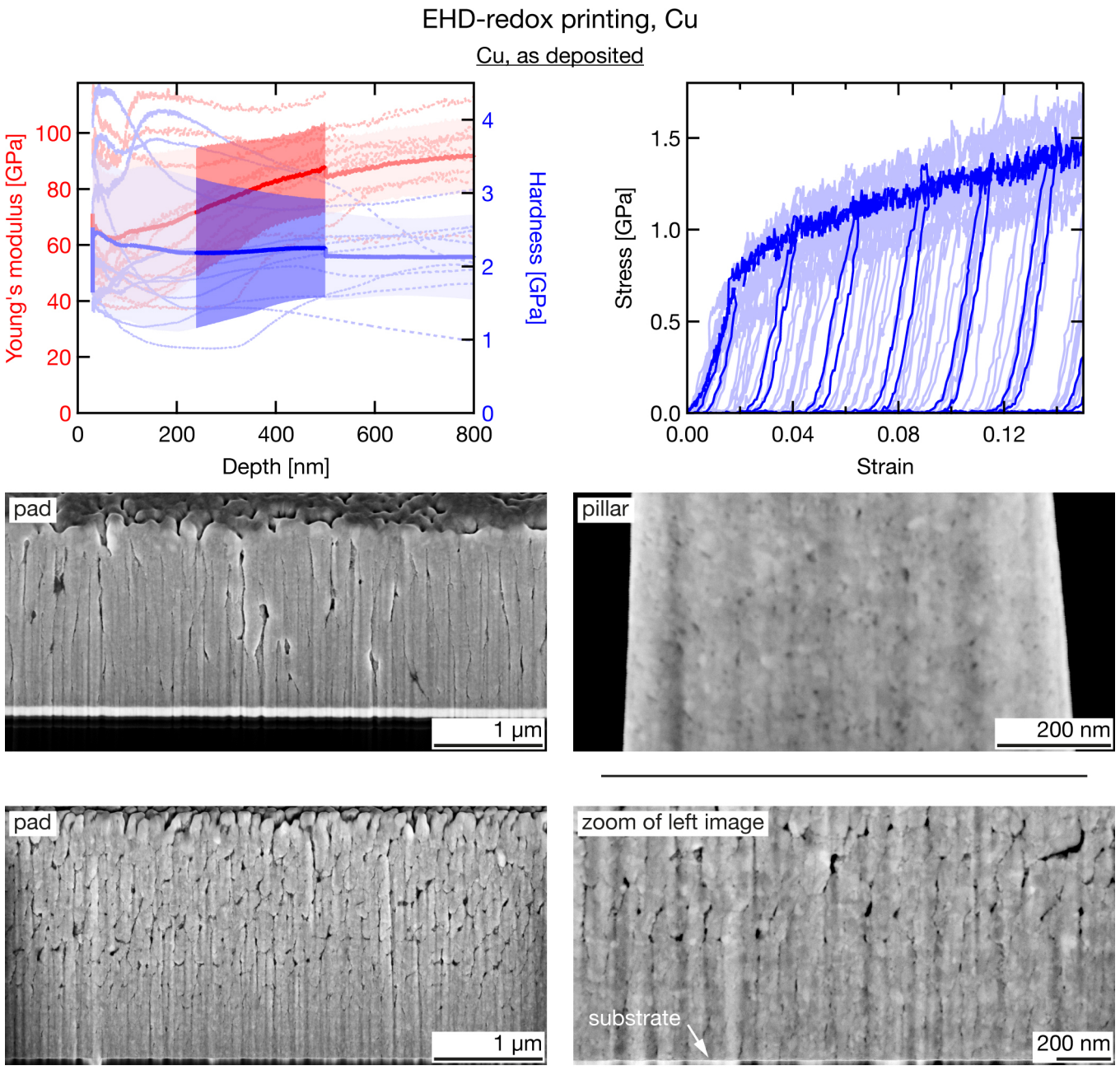

Figure S17: Electrohydrodynamic redox printing (EHD-RP) of Cu. Left: cross-sections of two pads printed by EHD-RP. The top pad shows vertical gaps instead of the nanoscale pores observed in the pillar (middle right). The bottom pad shows initial growth of Cu with high density. The zoomed image of this pad (bottom right) shows only a small number of nanoscale pores. Starting at a certain height, porosity increases as the growth parameters apparently result in less stable deposition.

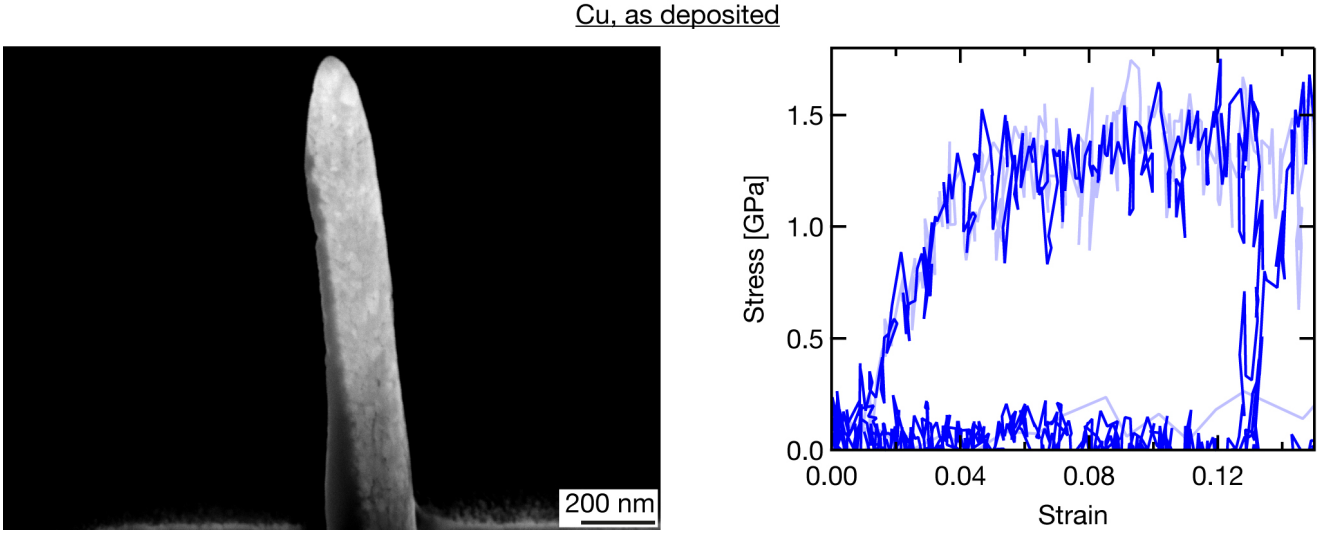

Figure S18: Electrohydrodynamic redox printing (EHD-RP) of Cu. Representative cross-section and microcompression data for two Cu pillars of 160 and 177 nm in diameter.

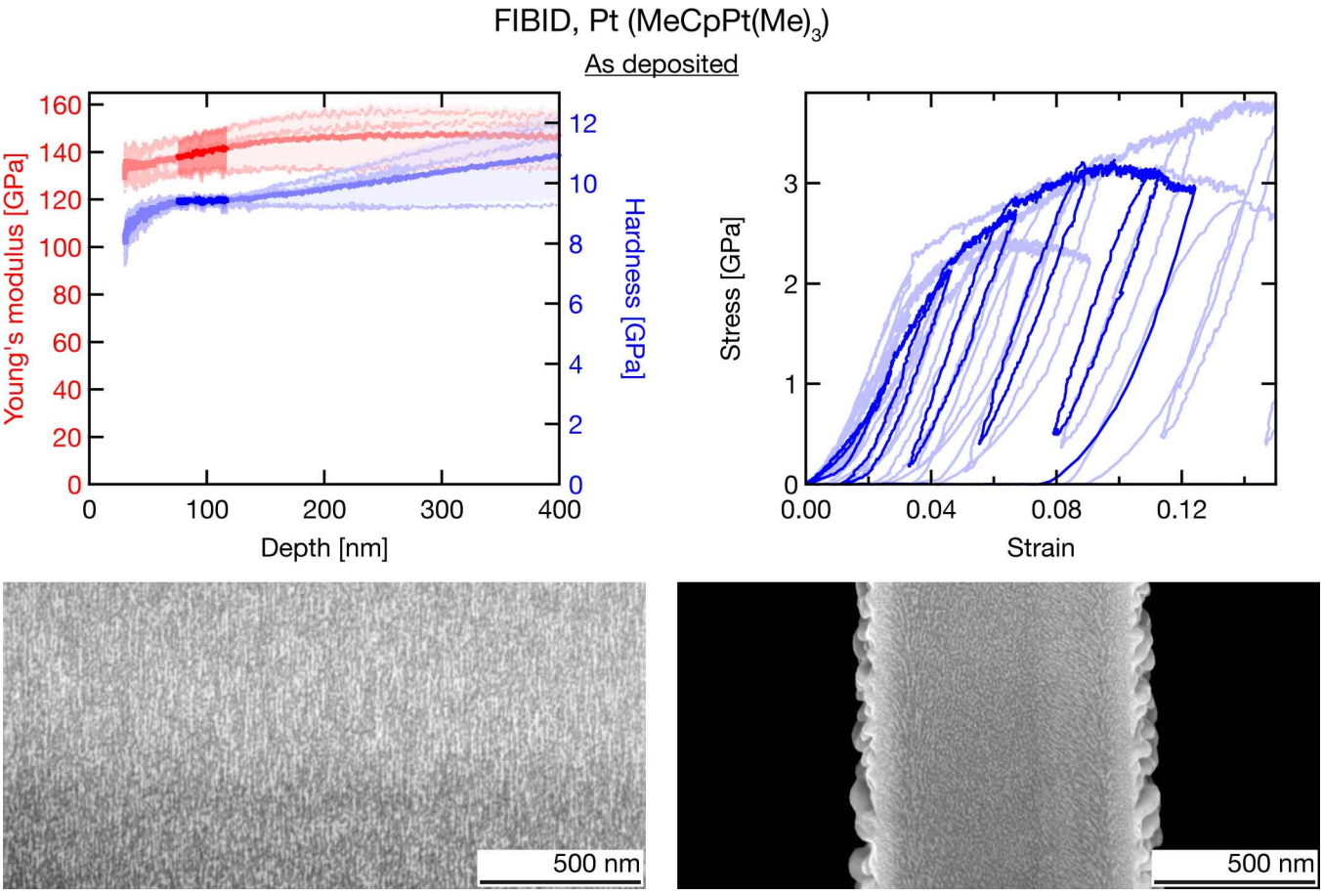

Figure S19: Focused ion beam-induced deposition (FIBID) of Pt ($MeCpPt(Me)_3$).

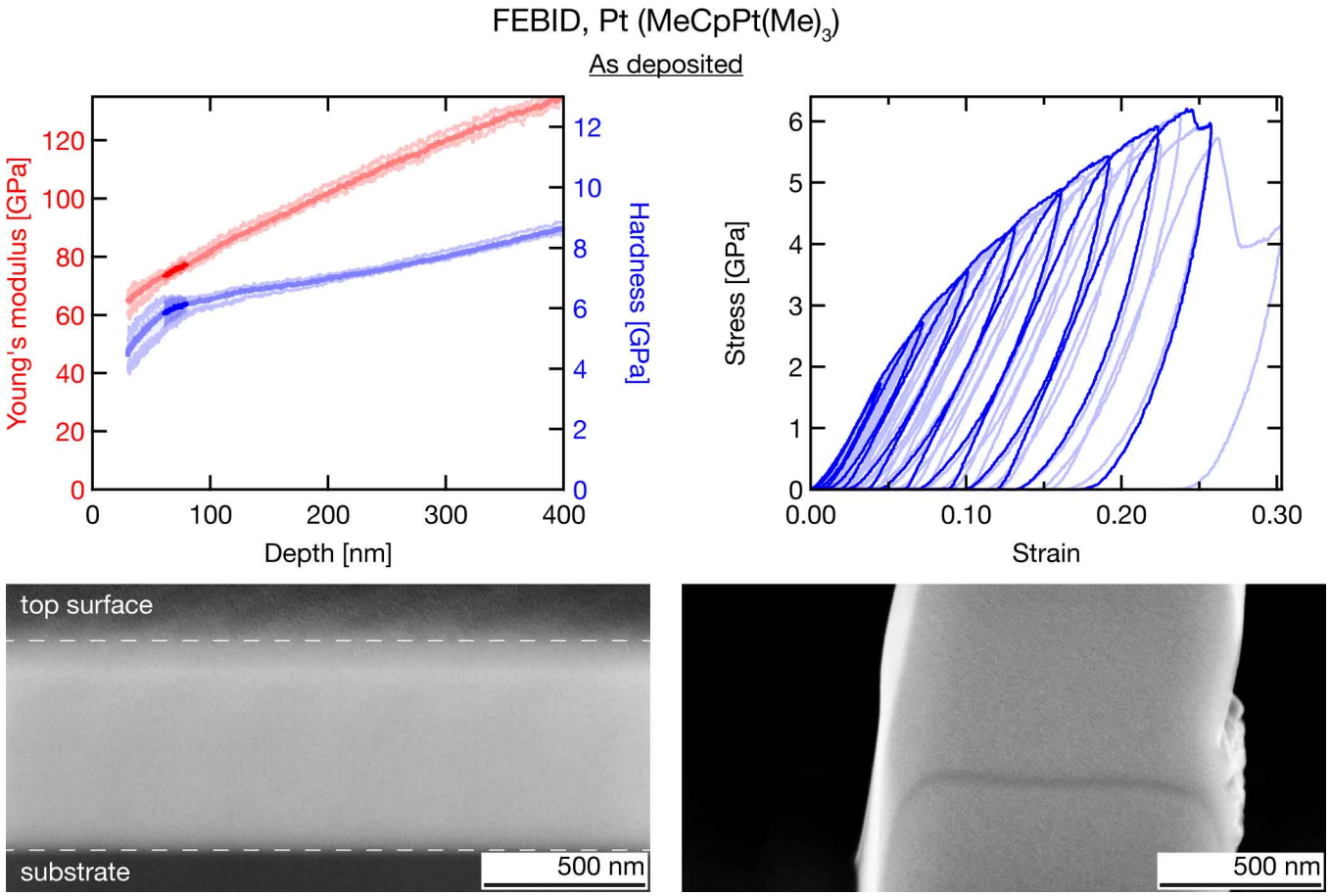

Figure S20: Focused electron beam-induced deposition (FEBID) of Pt ($MeCpPt(Me)_3$). The line feature seen in the pillar cross section is due to an interruption of the automated exposure pattern to mark the smooth growth front at this moment.

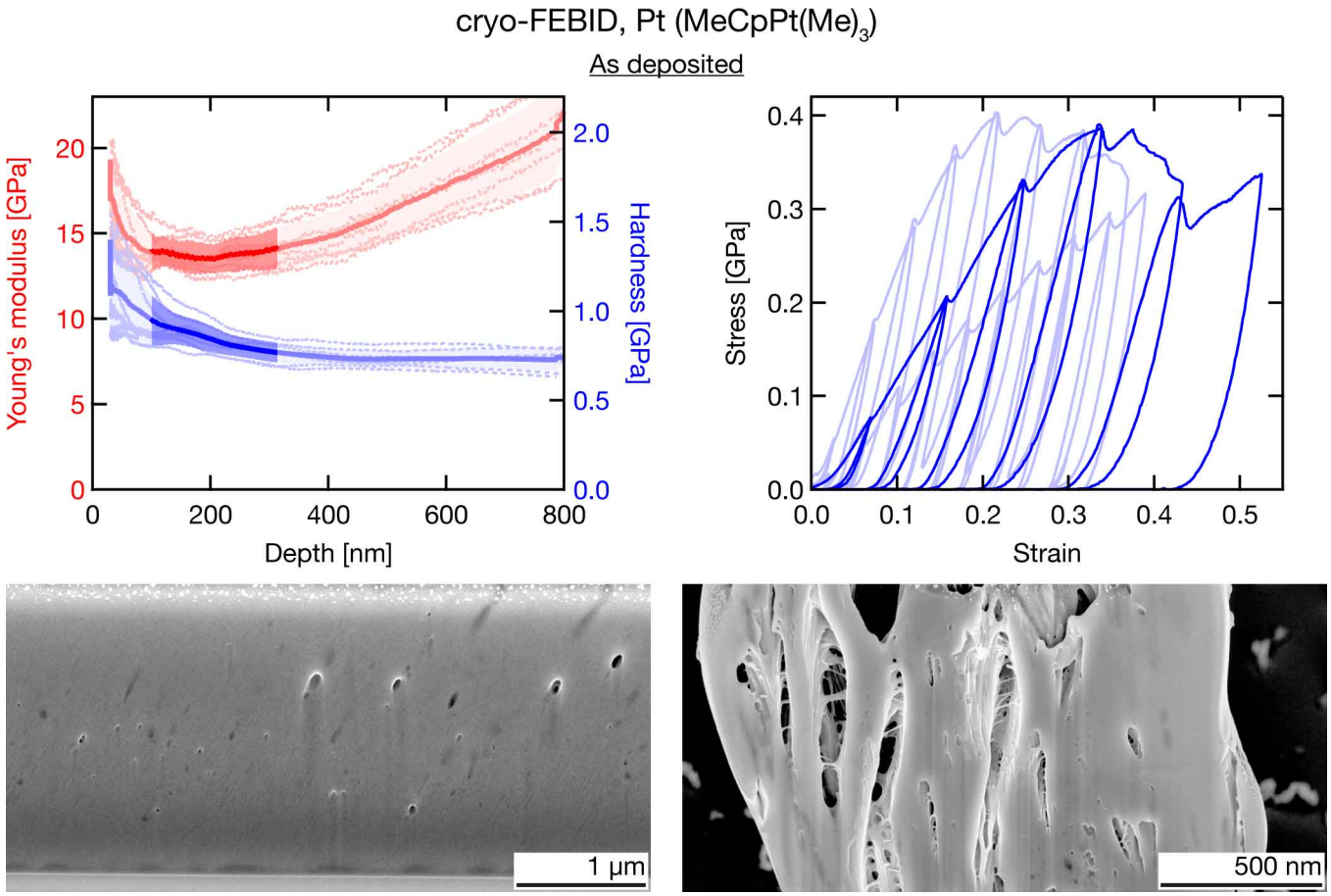

Figure S21: Focused electron beam-induced deposition at cryogenic temperatures (cryo-FEBID) of Pt ($MeCpPt(Me)_3$).

S4 Mechanical literature data of thin films

Table S3: **Mechanical literature data of thin films.** Literature values for E, H (measured by nanoindentation, Berkovich indenter) and σ_y (measured by microcompression and microtension) of polycrystalline thin films fabricated by traditional deposition techniques (PVD and electrodeposition). The data measured for the materials deposited by the studied small-scale AM methods was normalized to the values highlighted in **bold**.

Material	E [GPa]	H [GPa]	σ_y [GPa]
Ag	**80.5** [12] (bulk), ~80 [13,14]	0.7 – 1.5 [13,14] , **1.2**	N/A
Au	**80.2** [12] (bulk), 55 – 88.6 [15,16]	1 – 2 [15,16], **1.2**	0.04 – 0.8 [17–20]
Cu	**125** [12] (bulk), 88 – 135 [21–24]	1.6 – 3.5 [22,24–26], **2**	0.2 – 1.2 [27–29]
Pt	**174** [12] (bulk), 150 – 178 [30–32]	1.5 – 8.6 [32–34], **4**	N/A
amorphous C	132 (bulk), 40 – 760 [35–37]	5 – 30 [35,36]	7 [37]

References

[1] A. Piqué, R. C. Y. Auyeung, A. T. Smith, H. Kim, S. A. Mathews, N. A. Charipar, M. A. Kirleis, *Proc. SPIE* **2013**, *8608*, 86080K.

[2] E. Breckenfeld, H. Kim, R. Auyeung, N. Charipar, P. Serra, A. Piqué, *Appl. Surf. Sci.* **2015**, *331*, 254.

[3] M. G. Stanford, B. B. Lewis, J. H. Noh, J. D. Fowlkes, N. A. Roberts, H. Plank, P. D. Rack, *ACS Appl. Mater. Interfaces* **2014**, *6*, 21256.

[4] B. Geier, C. Gspan, R. Winkler, R. Schmied, J. D. Fowlkes, H. Fitzek, S. Rauch, J. Rattenberger, P. D. Rack, H. Plank, *J. Phys. Chem. C* **2014**, *118*, 14009.

[5] M. M. Shawrav, P. Taus, H. D. Wanzenboeck, M. Schinnerl, M. Stöger-Pollach, S. Schwarz, A. Steiger-Thirsfeld, E. Bertagnolli, *Sci. Rep.* **2016**, *6*, 34003.

[6] M. V. Puydinger dos Santos, A. Szkudlarek, A. Rydosz, C. Guerra-Nuñez, F. Béron, K. R. Pirota, S. Moshkalev, J. A. Diniz, I. Utke, *Beilstein J. Nanotechnol.* **2018**, *9*, 91.

[7] J. Pablo-Navarro, C. Magén, J. M. de Teresa, *ACS Appl. Nano Mater.* **2018**, *1*, 38.

[8] T. Y. Choi, D. Poulikakos, C. P. Grigoropoulos, *Appl. Phys. Lett.* **2004**, *85*, 13.

[9] P. Buffat, J.-P. Borel, *Phys. Rev. A* **1976**, *13*, 2287.

[10] D. Tabor, *Rev. Phys. Technol.* **1970**, *1*, 145.

[11] H. M. Jaeger, S. R. Nagel, R. P. Behringer, *Rev. Mod. Phys.* **1996**, *68*, 1259.

[12] W. Köster, H. Franz, *Metall. Rev.* **1961**, *6*, 1.

[13] A. Shugurov, A. Panin, C. Hui-Gon, K. Oskomov, *Sci. Technol. 2004. KORUS 2004. Proceedings. 8th Russ. Int. Symp.* **2004**, *3*, 168.

[14] A. Panin, A. Shugurov, K. Oskomov, *Phys. Solid State* **2005**, *47*, 2055.

[15] S. Okuda, M. Kobiyama, T. Inami, *Mater. Trans. JIM* **1999**, *40*, 412.

[16] A. A. Volinsky, N. R. Moody, W. W. Gerberich, *J. Mater. Res.* **2004**, *19*, 2650.

[17] R. D. Emery, G. L. Povirk, *Acta Mater.* **2003**, *51*, 2067.

[18] R. D. Emery, G. L. Povirk, *Acta Mater.* **2003**, *51*, 2079.

[19] C. Y. Chen, M. Yoshiba, T. Nagoshi, T. F. M. Chang, D. Yamane, K. Machida, K. Masu, M. Sone, *Electrochem. commun.* **2016**, *67*, 51.

[20] S. Yanagida, T.-f. M. Chang, C.-y. Chen, T. Nagoshi, D. Yamane, K. Machida, K. Masu, M. Sone, *Microelectron. Eng.* **2017**, *174*, 6.

[21] T.-H. Fang, W.-J. Chang, *Microelectron. Eng.* **2003**, *65*, 231.

[22] L. Lu, R. Schwaiger, Z. W. Shan, M. Dao, K. Lu, S. Suresh, *Acta Mater.* **2005**, *53*, 2169.

[23] S. H. Hong, K. S. Kim, Y. M. Kim, J. H. Hahn, C. S. Lee, J. H. Park, *Compos. Sci. Technol.* **2005**, *65*, 1401.

[24] S.-Y. Chang, T.-K. Chang, *J. Appl. Phys.* **2007**, *101*, 033507.

[25] D. Beegan, S. Chowdhury, M. T. Laugier, *Surf. Coatings Technol.* **2003**, *176*, 124.

[26] D. Beegan, S. Chowdhury, M. T. Laugier, *Surf. Coatings Technol.* **2007**, *201*, 5804.

[27] M. Dao, L. Lu, Y. F. Shen, S. Suresh, *Acta Mater.* **2006**, *54*, 5421.

[28] D. Jang, C. Cai, J. R. Greer, *Nano Lett.* **2011**, *11*, 1743.

[29] M. Mieszala, G. Guillonneau, M. Hasegawa, R. Raghavan, J. M. Wheeler, S. Mischler, J. Michler, L. Philippe, *Nanoscale* **2016**, *8*, 15999.

[30] A. S. Darling, *Res. Lab. Johnson Matthey Co Ltd.* **1966**, 14.

[31] J. Merker, D. Lupton, M. Töpfer, H. Knake, *Platin. Met. Rev.* **2001**, *45*, 74.

[32] H. Nili, S. Walia, M. Bhaskaran, S. Sriram, *J. Appl. Phys.* **2014**, *116*, 163504.

[33] S. Mall, H. Lee, K. D. Leedy, R. A. Coutu, in *Part B Magn. Storage Tribol. Manuf. Tribol. Nanotribology; Eng. Surfaces; Biotribology; Emerg. Technol. Spec. Symp. Contact Mech. Spec. Symp. Nanotribology*, ASME, pages 1377–1378.

[34] J. Mencik, M. V. Swain, *MRS Proc.* **1994**, *356*, 729.

[35] X. Jiang, K. Reichelt, B. Stritzker, *J. Appl. Phys.* **1989**, *66*, 5805.

[36] M. Weiler, S. Sattel, T. Giessen, K. Jung, H. Ehrhardt, V. S. Veerasamy, J. Robertson, *Phys. Rev. B* **1996**, *53*, 1594.

[37] S. Cho, I. Chasiotis, T. A. Friedmann, J. P. Sullivan, *J. Micromechanics Microengineering* **2005**, *15*, 728.